This paper appears in IEEE/ASME Transactions on Mechatronics, 2019
DOI: 10.1109/TMECH.2019.2930732

An Integrator-Backstepping Control Approach for 3D Needle Steering

Bita Fallahi, Michael Waine, Carlos Rossa, Ron Sloboda, Nawaid Usmani, and Mahdi Tavakoli

***Abstract*—In this paper, we design a set of 2D needle steering controllers used to minimize the 3D deflection of a flexible, bevel-tipped needle. The controllers are based on a nonlinear design tool known as integrator-backstepping. The needle's deflection is split into its two 2D planar problems, each of which is then governed by its own, separate controller. One controller, called Vertical Deflection Control (VDC), steers the needle so that it deflects primarily along the vertical plane. The second controller, called Horizontal Deflection Control (HDC), steers the needle so that it deflects primarily along the horizontal plane. Our 3D steering algorithm combines the effect of these two controllers based on the current magnitude of the deflection along each plane. Using an 18 gauge brachytherapy needle, we tested our proposed method on a phantom tissue composed of liquid plastic, and a two-layer biological tissue formed of gelatin and *ex-vivo* beef. Without needle steering, the average needle deflection was 11.2 mm. Using the proposed 3D needle steering technique, the deflection decreased to an average of 0.5 mm.**

I. Introduction

A. Needle Steering Problem

Needle insertion is a standard type of medical procedure with many different applications. While needle insertion is commonly used in vaccinations and intravenous line insertions, with the improvement in medical imaging and technology its role has expanded to include procedures such as biopsies, brachytherapy, and regional anesthesia. In this paper, we focus our discussion on a specific needle insertion application known as permanent prostate brachytherapy (PPB), a treatment for early-stage prostate cancer [1]. However, the techniques discussed here can be applied to any form of deep-tissue needle insertion procedure.

PPB, when appropriately performed, has shown to be highly successful in treating early-stage prostate cancer [2]. The procedure involves the use of long, bevel-tipped needles containing radioactive seeds. The needles are inserted through the perineum into the prostate gland. The seeds are then ejected and permanently implanted into the patient's prostate. These brachytherapy seeds are used to apply a pre-specified dosage of radiation to the prostate gland, destroying cancerous cells over the course of several months. It is crucial that the seeds are deposited near their target locations to achieve the proper radiation dose since errors with respect to radiation exposure can lead to the remission of cancerous cells. Therefore, the needles must travel to their target locations with high precision to allow for proper seed placement.

Bevel-tipped needles are useful in the sense that they are easy to manufacture and can be designed with a hollow interior to allow for drugs or fluids to be injected or ejected from the needle [3]. The design also allows the needle to maintain a sharp tip that can be effectively advanced through multiple tissue layers. However, the bevel results in an asymmetrical tip which leads to an imbalance of tip forces [4], [5], which causes the needle to deflect during the insertion process.

There are different challenges involved in two dimensional (2D) and three dimensional (3D) needle steering problem [6]. There have been a variety of studies performed on 2D needle steering and the development of 2D needle steering robots. Most methods perform the needle through axial needle rotation, which allows the needle follows the desired trajectory. For example, the needle steering robot developed by Neubach *et al.* [7] made use of a spring-based interaction model to inform their path planning algorithm. DiMaio and Salcudean [8] developed a system that made use of repulsion and attraction potentials to steer the needle. Kallem and Cowan [9] developed a feedback linearization-based controller for out-of-plane deflection minimization. Authors in [10] used an adaptive controller to stabilize the needle in one plane. Fallahi *et al.* [11] designed a non-model-based sliding controller, and Khadem *et al.* [12] proposed a novel dynamical model to be used in controlling the in-plane needle deflection via axial rotations. In these studies, the needle has either been assumed to remain in a single plane, or controlled to deflect within one plane without consideration of the needle's deflection within the other plane. However, factors such as tissue deformation can influence the needle's trajectory and lead to noticeable out-of-plane deflection. As well, deflection outside of a single plane is nearly inevitable unless the needle is completely stopped during the rotation process.

Some research groups have explored 3D needle steering strategies. Studies have been performed on laterally adjusting an external template or applying lateral forces at the needle base to affect the needle's trajectory during insertion, including [13]–[16]. Other groups have focused on rotation-based 3D needle steering approaches, which typically allow for a more compact device. However, many performing research this area have focused on experiments utilizing thin, nitinol wire as

This work was supported by the Natural Sciences and Engineering Research Council (NSERC) of Canada under grant CHRP 446520, the Canadian Institutes of Health Research (CIHR) under grant CPG 127768, and by the Alberta Innovates - Health Solutions (AIHS) under grant CRIO 201201232.

Bita Fallahi, Michael Waine and Mahdi Tavakoli (Corresponding Author) are with the Department of Electrical and Computer Engineering, University of Alberta, AB, Canada T6G 1H9. E-mail: fallahi@ualberta.ca; mwaine@ualberta.ca; mahdi.tavakoli@ualberta.ca

Carlos Rossa is with the Faculty of Engineering and Applied Science, Ontario Tech University, Oshawa, ON, Canada . E-mail: carlos.rossa@uoit.ca

Ron Sloboda and Nawaid Usmani are with the Cross Cancer Institute and the Department of Oncology, University of Alberta, Edmonton, AB, Canada T6G 1Z2. E-mail: ron.sloboda@albertahealthservices.ca; nawaid.usmani@albertahealthservices.ca

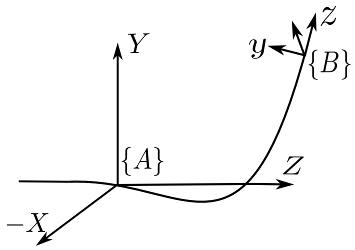

Fig. 1. The needle shown in 3D space. The frame $\{A\}$ is the fixed frame and the moving frame $\{B\}$ is attached to the needle tip. The needle is inserted along the z-axis.

opposed to clinical needles, [17]–[21]. This can lead to the reliance of needle steering paths that are impossible in hospital settings due to the stiffness of clinical needles.

Similarly, some groups have focused on the use of pre-bent or pre-curved needles [20], [21], or needles containing internal concentric tubes to assist with needle steering [22]–[24]. However, rotating these type of needles could potentially cause excessive tissue cutting and trauma. Additionally, in PPB, the interior of the needle is filled with the radioactive seeds, preventing other types of steering devices, such as actively controlled cannulas, be inserted within.

Some groups such as [17]–[19], [25] make use of duty-cycling controllers, in which the needle is inserted with periods of no rotation or periods of continual rotation to control the degree of deflection at various stages of the insertion process [26]. Some duty-cycling controllers make use of rotation velocities of up to five rotations per second [17]. Yan *et al.* have shown that the use of rotational drilling can be used to reduce target movement and tissue deformation greatly [27], but we desire to reduce this type of "drilling" motion used in duty-cycling controllers since it could have significant effects on tissue trauma, swelling, and recovery. Instead, we want to focus on controlled, smaller-scale, slower rotations performed throughout the insertion process.

In this paper, we demonstrate a 3D needle steering algorithm based on the kinematic model of a flexible, bevel-tipped needle developed by Webster *et al.* [28], and developed in its current form by Kallem and Cowan [9]. The proposed controller attempts to reduce deflection in both the $x - z$ and $y - z$ planes simultaneously without requiring continuous rotation like many other steering methods. This is beneficial because it avoids requiring the needle to "drill" into the tissue. The relationship between continuous needle rotation, tissue trauma, and tissue recovery are not well-understood, and from a clinical perspective, it is sensible to avoid tissue damage as much as possible.

B. Contributions

The well-known integrator-backstepping technique is a non-linear design tool based on the proper selection of a Lyapunov function. The main premise is to divide the system into multiple cascaded subsystems which are easier to solve and fine-tune. Then, we gradually work back towards the original system to obtain the final controller design. Here, we employ this technique to design the controller. In [29] this technique is used for needle steering in 2D environment, however, there are two main differences between the controller proposed in [29] and the method presented here. First, the controller in [29] only considers the error compensation in 2D environment, whereas here, we extend the method to design a 3D controller. Secondly, the controller in [29] does not consider the bounds imposed on the transformed variables and the inherent saturation of the system variables. In the current method these effects are taken into account and new 2D controllers are designed and combined to control the needle's 3D tip path. The effect of state saturation and the convergence of each individual controller as well as the stability of both controllers operating together are shown and verified through simulations and experiments.

The rest of the paper is structured as follows. Section II describes the derivation of our steering algorithm and the controller design. Section III provides the analysis of the effects of the saturation on the stability. In Section IV, the needle steering robot used in this paper is shown, and an illustration of our experimental setup is provided. Simulation and experimental results are shown in Section V and in Section VI, the results are detailed and discussed. Conclusions are drawn in Section VII.

II. Integrator-Backstepping Controller

In this section, we discuss the development of our steering controllers derived using the nonlinear design technique known as integrator-backstepping. Our strategy makes use of two separate controllers, each designed to limit the needle's deflection to a single plane. By properly combining these two controllers, we can limit the needle's overall deflection. In Section II-A, we give a general overview of the integrator-backstepping technique applied in our needle steering application. In Section II-B, we call the controller designed to limit needle deflection to the vertical plane as Vertical Deflection Control (VDC) and the controller designed to limit needle deflection to the horizontal plane as Horizontal Deflection Control (HDC).

A. Needle Steering Control Using Integrator-Backstepping

The kinematics of a flexible bevel-tipped needle used in this paper are based on the bicycle model developed by Webster *et al.* [28] as

$$\dot{P} = R \begin{bmatrix} 0 \\ 0 \\ v \end{bmatrix} \tag{1a}$$

$$\dot{R} = R \begin{bmatrix} 0 & -u & 0 \\ u & 0 & -\kappa v \\ 0 & \kappa v & 0 \end{bmatrix} \tag{1b}$$

In this equation, the dot operator $\{\dot{}\}$ represents the first derivative with respect to time and the vector $P = [x,\ y,\ z]$ refers to the position of the needle tip and R is a 3×3 matrix representing the orientation of the moving frame B attached to the needle tip with respect to the fixed frame A, as shown in Fig. 1. The needle deflects along a curve defined by a radius of curvature κ. The values v and u are the insertion velocity and axial rotation velocity of the needle respectively, both of which are applied to the base of the needle by our needle steering robot. The variable u is the control input, and we assume that $v > 0$, since (1) is only valid for forward insertion of the needle, as opposed to needle retraction [28]. In this particular study, v is held constant throughout the entire insertion. Equation (2) is derived in its current-form by Kallem and Cowan [9] using the Z-Y-X fixed angles as generalized coordinates:

$$\begin{bmatrix} \dot{x} \\ \dot{y} \\ \dot{z} \\ \dot{\alpha} \\ \dot{\beta} \\ \dot{\gamma} \end{bmatrix} = \begin{bmatrix} \sin\beta & 0 \\ -\cos\beta\sin\alpha & 0 \\ \cos\alpha\cos\beta & 0 \\ \kappa\cos\gamma\sec\beta & 0 \\ \kappa\sin\gamma & 0 \\ -\kappa\cos\gamma\tan\beta & 1 \end{bmatrix} \begin{bmatrix} v \\ u \end{bmatrix} \tag{2}$$

which is valid in

$$\mathcal{U} = \{q \in \mathbb{R}^6 : \alpha, \gamma \in \mathbb{R}\text{mod}(2\pi), \beta \in (-\pi/2, \pi/2)\} \tag{3}$$

with $q = [x,\ y,\ z,\ \alpha,\ \beta,\ \gamma]$ where $\alpha,\ \beta,$ and γ refer to the yaw, pitch, and roll of the needle respectively. These are the Euler angles corresponding to the rotation matrix, representing the orientation of the frame attached to the needle tip. In general, the orientation of the moving frame can be obtained by three successive rotations about the axes of the fixed frame and the corresponding rotation matrix can be found by pre-multiplying of the three basic rotation matrices [30].

In the integrator-backstepping approach, a stabilizing control input can be found for a system of the form

$$\dot{\xi}_1 = f_1(\xi_1) + g_1(\xi_1)\xi_2 \tag{4a}$$
$$\dot{\xi}_2 = f_2(\xi_1, \xi_2) + g_2(\xi_1, \xi_2)\xi_3 \tag{4b}$$
$$\dot{\xi}_3 = f_3(\xi_1, \xi_2, \xi_3) + g_3(\xi_1, \xi_2, \xi_3)u \tag{4c}$$

where ξ_1, ξ_2 and ξ_3 represent the state variables and u represents the control input.

A control law that stabilizes the above system to the origin can be derived in three steps, described in [31]. Note that stabilizing the system to a non-zero constant can be done by shifting the states and rewriting the equations as a zero stabilization problem. Step 1 starts with (4a). Viewing ξ_2 as the input, we design the feedback control $\xi_2 = \phi(\xi_1)$ to stabilize (4a) to the origin $\xi_1 = 0$ and such that the Lyapunov function $V_1(\xi_1)$ is positive definite and radially unbounded, and $\dot{V}_1(\xi_1)$ is at least negative semi-definite. In step 2, the subsystem composed of (4a) and (4b) is considered and having ξ_3 as the input a controller is designed using the associated Lyapunov function $V_2(\xi_1, \xi_2)$ and in step 3, the control signal u is designed for the system (4a), (4b) and (4c) using the Lyapunov function $V_3(\xi_1, \xi_2, \xi_3)$. These steps will now be applied to construct the VDC and HDC controllers. In the sequel, all the values k_i and $c_i, (i = 1, 2, ...)$ are positive constant parameters which will be designed accordingly.

B. Vertical Deflection Control (VDC)

In order to limit the needle to the vertical plane, thereby reducing deflection along the x-axis, we must develop a control input that brings the deflection x and the effect of the bevel orientation to zero. This can be performed by applying integrator-backstepping to the following subsystem:

$$\dot{x} = v\sin\beta \tag{5a}$$
$$\dot{\beta} = \kappa v\sin\gamma \tag{5b}$$
$$\dot{\gamma} = -\kappa v\cos\gamma\tan\beta + u \tag{5c}$$

Using the change of variable $\xi_1 = x$, $\xi_2 = \sin\beta$ and $\xi_3 = \sin\gamma$, we can re-write (5a)-(5c) in (3) as

$$\dot{\xi}_1 = v\xi_2 \tag{6a}$$
$$\dot{\xi}_2 = \kappa v\left(\sqrt{1-\xi_2^2}\right)\xi_3 \tag{6b}$$
$$\dot{\xi}_3 = -\kappa v\xi_2(1-\xi_3^2) \pm \left(\sqrt{1-\xi_2^2}\right)u \tag{6c}$$

The above system is now in strict feedback form. We can begin deriving the control law to stabilize the system to the origin. It should be noted that this change of variable bounds the system variables as $|\xi_2| < 1$ and $|\xi_3| < 1$, for which the boundedness of the states' references $|\xi_{2ref}|$ and $|\xi_{3ref}|$ should be taken into account. Let the upper bounds of ξ_{2ref} and ξ_{3ref} be $0 < \xi_2^* < 1$ and $0 < \xi_3^* < 1$, respectively.

Step 1: Start with (6a). Choosing the Lyapunov function $V_1(\xi_1) = k_1\xi_1\arctan(\kappa\xi_1)$, which is positive definite and radially unbounded, we can select

$$\xi_{2ref} = \phi(x) = -c_1\arctan(\kappa\xi_1) \tag{7}$$

to stabilize (6a) to the origin. Defining

$$z_1 = \xi_2 - \xi_{2ref} \tag{8a}$$
$$\dot{z}_1 = \kappa v\left(\sqrt{1-\xi_2^2}\right)\xi_3 + \frac{c_1\kappa v\xi_2}{1+(\kappa\xi_1)^2} \tag{8b}$$

the time derivative of V_1 can be written as

$$\dot{V}_1 = -W + k_1 v z_1\left(\arctan(\kappa\xi_1) + \frac{\kappa\xi_1}{1+(\kappa\xi_1)^2}\right) \tag{9}$$

with $W = k_1 v c_1\arctan(\kappa\xi_1)\left(\arctan(\kappa\xi_1) + \frac{\kappa\xi_1}{1+(\kappa\xi_1)^2}\right) > 0$.

Remark: c_1 should be selected such that $|c_1\arctan(\kappa\xi_1)| < \xi_2^*$ or equivalently

$$c_1 < \frac{\xi_2^*}{\arctan(\kappa\xi_{1max})} \tag{10}$$

where ξ_{1max} is the maximum possible initial deflection along the x axis. With this selection, since ξ_2 is also bounded, z_1 will be bounded as well.

Step 2: Next, consider the subsystem composed of (6a) and (6b). Select the Lyapunov function:

$$V_2 = V_1 + \frac{k_3}{2(k_2^2 - z_1^2)} \tag{11}$$

which is positive definite for $|z_1| < k_2$. As it will be shown in section III-A, this function ensures k_2 to be the desired hard bound on z_1, which can be achieved by proper selection of the parameters. Taking the time derivative of V_2 we have:

$$\dot{V}_2 = z_1\left(k_1 v\arctan(\kappa\xi_1) + \frac{k_1 v\kappa\xi_1}{1+(\kappa\xi_1)^2} + \frac{k_3\dot{z}_1}{(k_2^2 - z_1^2)^2}\right) - W \tag{12}$$

Viewing ξ_3 as an independent input for the subsystem, we can find a state feedback control law $\xi_{3ref} = \phi(\xi_1, z_1)$ to stabilize the subsystem to the origin. By selecting $k_1 = \kappa$, a stabilizing control law can be selected as

$$\begin{aligned}\xi_{3ref} = &\frac{1}{\sqrt{1-\xi_2^2}}\left(-c_2 z_1 - \frac{c_1\xi_2}{1+(\kappa\xi_1^2)^2}\right.\\ &\left.-\frac{(k_2^2-z_1^2)^2}{k_3}\left(\arctan(\kappa\xi_1)+\frac{\kappa\xi_1}{1+(\kappa\xi_1)^2}\right)\right)\end{aligned} \tag{13}$$

To guarantee the upper bound $|\xi_{3ref}| < \xi_3^*$, the following constraint should be satisfied:

$$c_2k_2 + c_1 + \frac{k_2^2}{k_3}\left(\frac{\pi+\kappa}{2}\right) < \xi_3^2\sqrt{1-(\xi_2^*+k_2)^2} \tag{14}$$

In this equation ξ_2^* and k_2 should be selected such that $\xi_2^* + k_2 < 1$

Step 3: Define

$$z_2 = \xi_3 - \xi_{3ref} \tag{15a}$$

$$\dot{z}_2 = -\kappa v\xi_2(1-\xi_3^2) \pm \left(\sqrt{1-\xi_2^2}\right)u - \dot{\xi}_{3ref} \tag{15b}$$

Using the Lyapunov function:

$$V_3 = V_{2x} + \frac{k_5}{2\,(k_4^2 - z_2^2)} \tag{16}$$

which is positive definite for $|z_2| < k_4$, the stabilizing control law u_x for the subsystem described in (5a)-(5c) is obtained as:

$$\begin{aligned}u_x = &\frac{\pm 1}{\sqrt{1-\xi_3^2}}\left[-c_3 z_2 + \dot{\xi}_{3ref} + \frac{\kappa v\xi_2(1-\xi_3^2)}{\sqrt{1-\xi_2^2}}\right.\\ &\left.-\frac{(k_4^2-z_2^2)^2}{k_5}\left(\frac{k_3 z_1}{(k_2^2-z_1^2)}\right)\right]\end{aligned} \tag{17}$$

The $\pm$ sign in (17) is related to sign$(\cos\gamma)$, which can be selected accordingly. In section III-A it will be shown that k_4 is the hard bound on z_2. Moreover, the value of k_4 and ξ_3^* should be selected such that $\xi_3^* + k_4 < 1$, which also ensures that in (17), $\sqrt{1-\xi_3^2} \neq 0$. Then we have the time derivative of V_3 as:

$$\dot{V}_3 = -W - \frac{c_2k_3z_1^2}{(k_2^2-z_1^2)^2} - \frac{c_3k_5z_2^2}{(k_4^2-z_2^2)^2} < 0 \tag{18}$$

which shows the convergence of the deflection to the origin.

C. Horizontal Deflection Control (HDC)

Analogous to the previous section, a similar strategy is used to develop a controller that limits the needle to the horizontal plane. To this end, here we write the rotation matrix in (1) using the Z-X-Y fixed angles. The system equations can be re-written as

$$\dot{x} = v\sin\beta'\cos\alpha' \tag{19a}$$

$$\dot{y} = -v\sin\alpha' \tag{19b}$$

$$\dot{z} = v\cos\alpha'\sin\gamma' \tag{19c}$$

$$\dot{\alpha}' = \kappa v\cos\gamma' \tag{19d}$$

$$\dot{\beta}' = \kappa v\sin\gamma'\sec\alpha' \tag{19e}$$

$$\dot{\gamma}' = \kappa v\tan\alpha' + u \tag{19f}$$

which is valid in

$$\mathcal{U}' = \{q \in \mathbb{R}^6 : \alpha', \gamma' \in \mathbb{R}\mathrm{mod}(2\pi), \beta' \in (-\pi/2, \pi/2)\} \tag{20}$$

The relation between $[\alpha, \beta, \gamma]$ and $[\alpha', \beta', \gamma']$ can be found as

$$\begin{aligned}\alpha' &= \arcsin(\sin\alpha\cos\beta)\\ \beta' &= \arccos(\frac{\cos\alpha\cos\beta}{\cos\alpha'})\\ \gamma' &= \gamma + \arctan(\sin\alpha'\tan\beta')\end{aligned} \tag{21}$$

Using the change of variable $[\zeta_1,\ \zeta_2,\ \zeta_3] = [y, -\sin\alpha', -\cos\gamma']$, we have

$$\dot{\zeta}_1 = v\zeta_2 \tag{22a}$$

$$\dot{\zeta}_2 = \kappa\sqrt{1-\zeta_1^2}\zeta_3 \tag{22b}$$

$$\dot{\zeta}_3 = \frac{-\kappa v(1-\zeta_3^2)}{\sqrt{1-\zeta_2^2}} \pm \sqrt{1-\zeta_3^2}u \tag{22c}$$

Comparing (22) and (6) it is clear the using the new variables, the HDC controller can be designed using the same procedure presented for VDC, and the controller can be written as

$$\begin{aligned}u_y = &\frac{\pm 1}{\sqrt{1-\zeta_3^2}}\left[-c_3 z_2' + \dot{\zeta}_{3ref} + \frac{\kappa v\zeta_2(1-\zeta_3^2)}{\sqrt{1-\zeta_2^2}}\right.\\ &\left.-\frac{(k_4^2-z_2'^2)^2}{k_5}\left(\frac{k_3 z_1'}{(k_2^2-z_1'^2)}\right)\right]\end{aligned} \tag{23}$$

in which $z_1' = \zeta_2 - \zeta_{2ref}$ and $z_2' = \zeta_3 - \zeta_{3ref}$. This procedure gives $\zeta_{3ref} = \cos\gamma_d'$, which is related to $\cos\gamma_d$ as

$$\cos\gamma_d = \frac{\zeta_{3ref} \pm \sqrt{1-\zeta_{3ref}^2}(1+\sin^2\alpha'\tan^2\beta')}{\sqrt{1+\sin^2\alpha'\tan^2\beta'}} \tag{24}$$

III. Bounds and Saturation

Since the accelerations along the x and y axes are related to $\sin(\gamma)$ and $\cos(\gamma)$, respectively, they are naturally bounded to $[-1, 1]$. Moreover, from (17) and (23), implementing any of these controllers individually requires to bound the magnitude of the acceleration to some value less than one. In this section, we analyze the effect of the acceleration saturation on the stability of the system. Since the control inputs u_x and u_y have the same structure, in the sequel we provide the analysis for the x direction, however, the same argument applies to the y direction.

A. Bounds on the Variables

In the previous section it is assumed that k_2 and k_4 are the hard bounds on z_1 and z_2, respectively. To show this, we use the Lyapunov function (16). Denoting

$$\mathcal{X} = \{\xi_1,\ z_1,\ z_2\} \tag{25a}$$

$$\mathcal{C} = \{\mathcal{X} \in \mathbb{R} : |z_1| < k_2,\ |z_2| < k_4\} \tag{25b}$$

and the boundaries and the interior of $\mathcal{C}$ as $\partial\mathcal{C}$ and Int$\{C\}$, respectively, we have

$$\inf_{x\in\text{Int}\{\mathcal{C}\}} V_3(x) \geq 0 \tag{26a}$$

$$\lim_{x\to\partial\mathcal{C}} V_3(x) = \infty \tag{26b}$$

$$\dot{V}_3 \leq 0 \quad x\in\text{Int}\{\mathcal{C}\} \tag{26c}$$

In [32] it is shown that such a function is a control barrier function, for which Int$\{\mathcal{C}\}$ is invariant. Equivalently, any state starting from Int$\{\mathcal{C}\}$ remains in this region and guarantees the hard bounds on z_1 and z_2.

B. Effect of Saturation

According to the change of variables introduced in II-B, the new states ξ_2 and ξ_3 as well as their references ξ_{2ref} and ξ_{3ref} are upper bounded. Any reference value greater than one produces large control inputs causing the needle to rotate constantly and lose the control over the system. This can be avoided by proper selection of the design parameters to keep the reference values in the desired region. To this end the design parameters c_1, c_2 and k_2 should satisfy (10) and (14), which impose very strict constraints on these parameters. From (14) having c_1 less than one is not desirable as it slows down the deflection convergence. Another solution is to saturate the reference values manually. Having $|\xi_{3ref}| = \xi_3^*$ keeps the system in saturation to use the system's maximum capacity. In this case, the stability and convergence analysis should be performed in the presence of the state saturation. Consider the following assumptions.

Assumptions: To simplify the analysis assume k_3 in (13) is large so we can neglect the last term on the right-hand side of (13). Whenever $|\xi_{3ref}| > \xi_3^*$ let $\xi_{3ref} = sgn(\xi_{3ref})\xi_3^*$ and $\dot{\xi}_{3ref} = 0$. Assume that using these values and the control signal (17), $z_2 \to 0$ and consequently $\xi_3 = \xi_{3ref}$.

Case 1: If $\xi_{3ref} > \xi_3^*$, using (13) and (8b) we have $z_1 < -\dot{z_1}$, which for $z_1 > 0$ leads to $z_1\dot{z}_1 < 0$. If $z_1 < 0$ and $|\dot{\xi}_{2ref}| < \sqrt{1-\xi_2^2}\xi_3^*$ or $\dot{\xi}_{2ref} < -\sqrt{1-\xi_2^2}\xi_3^* > 0$ then $\dot{z}_1 < 0$ and again $z_1\dot{z}_1 < 0$. However, $|\dot{\xi}_{2ref}| > \sqrt{1-\xi_2^2}\xi_3^*$ and $\dot{\xi}_{2ref} > 0$, leads to $\dot{z}_1 > 0$. To overcome this case, we set $\xi_{2ref} = -\xi_2^*$ and $\dot{\xi}_{2ref} = 0$ until the states get out of this situation.

Case 2: If $\xi_{3ref} < -\xi_3^*$, using (13) and (8b) we have $z_1 > -\dot{z_1}$, which for $z_1 < 0$ leads to $z_1\dot{z}_1 < 0$. If $z_1 > 0$ and $|\dot{\xi}_{2ref}| < \sqrt{1-\xi_2^2}\xi_3^*$ or $\dot{\xi}_{2ref} > \sqrt{1-\xi_2^2}\xi_3^* > 0$ then $\dot{z}_1 > 0$ and again $z_1\dot{z}_1 < 0$. However, $|\dot{\xi}_{2ref}| > \sqrt{1-\xi_2^2}\xi_3^*$ and $\dot{\xi}_{2ref} < 0$, leads to $\dot{z}_1 < 0$. To overcome this case, we set $\xi_{2ref} = -\xi_2^*$ and $\dot{\xi}_{2ref} = 0$ until the states get out of this situation.

C. 3D Controller Design and Stability

In the previous sections, separate controllers were designed to control the needle deflection in vertical and horizontal planes. Having one control input, in this section we combine the two controllers. It should be noted that the two subsystems have needle tip orientation angles as state variables and therefore have dynamic coupling. The 3D controller introduced in this section deals with this coupling by simultaneously considering the effect of two subsystems. According to the design procedure of the 2D VDC (HDC), the last step determines and controls $\xi_3(\zeta_3)$, which is the needle acceleration along the $x(y)$ axis. Since ξ_3 (ζ_3) is related to $\sin\gamma$ $(\cos\gamma)$, it is possible to define a desired angle γ_d [33] so whenever $\gamma \to \gamma_d$, then ξ_3 (ζ_3) reaches its desired value, which leads to $z_2(z_2') \to 0$. However, since the trigonometric relation $\sin\gamma_d^2 + \cos\gamma_d^2 = 1$ should be satisfied, we select one axis as the primary axis and the other direction as the secondary and the find desired angle γ_d for the primary axis while considering the effect of the secondary desired value. The primary axis selection is done based on the greater deflection error; whichever axis with greater absolute error is the primary axis and the other is the secondary. Defining $\sin\gamma_d = \xi_{3ref}$ and $\cos\gamma_d = \xi'_{3ref}$, the desired angle γ_d is found as

$$\begin{cases} \text{if } \; x, & \gamma_d = \text{atan2}\left(\xi_{3ref}, \text{sgn}(\xi'_{3ref})\sqrt{\xi_3^{*2} - \xi_{3ref}^2}\right) \\ \text{if } \; y, & \gamma_d = \text{atan2}\left(\text{sgn}(\xi_{3ref})\sqrt{\xi_3^{*2} - \xi_{3ref}'^2}, \xi'_{3ref}\right) \end{cases} \tag{27}$$

with $\dot{\gamma}_d = 0$. Defining $z_{2\gamma} = \gamma - \gamma_d$, the control input

$$u = -c_4 z_{2\gamma} - \dot{\gamma}_d + \frac{\kappa v \xi_2 \sqrt{1-\xi_3^2}}{\sqrt{1-\xi_2^2}} \tag{28}$$

ensures $\gamma \to \gamma_d$. The *sgn* function in (27) takes the effect of the secondary axis into account, keeping the bevel orientation in a direction such that the accelerations along primary and secondary axes have their desired signs as determined by the 2D controllers. This is equivalent to having $\dot{V}_x < 0$ and $\dot{V}_y < 0$ and consequently decreasing the deflection error along both axes, however, it is clear that the acceleration along the primary axis is of greater magnitude, which makes the error to decrease faster in that direction. I should be noted that since this system does not have any equilibrium points, i.e., as long as the needle is being inserted, the velocities along the x and y axes have non-zero values, the proposed controller ensures the boundedness of the deflection error.

D. Practical Consideration

The algorithm presented in the previous section can be effective only if $\gamma \to \gamma_d$ to keep the bevel at the desired orientation to compensate the deflection error. The value γ_d should be updated at a slow rate since the radius of curvature κ limits the rate at which the deflection can be corrected. This imposes a natural delay on error compensation. Moreover, according to the dynamics of the system, the rotation transition time to steer γ to the desired value γ_d should be taken into account. If the changes in γ_d is faster than the settling time of γ, the designed strategy will not be effective. To overcome this, we update γ_d every T_s seconds, which should be larger than the settling time of the rotation loop. However, the value of T_s should be selected carefully as large values of T_s increase the bounds on the error.

In switching between the VDC and HDC controllers, we monitor the deflections along the x and y axes. If the deflection along x is higher than y, we use VDC as the primary controller and if the deflection along y is greater than x, we use HDC.

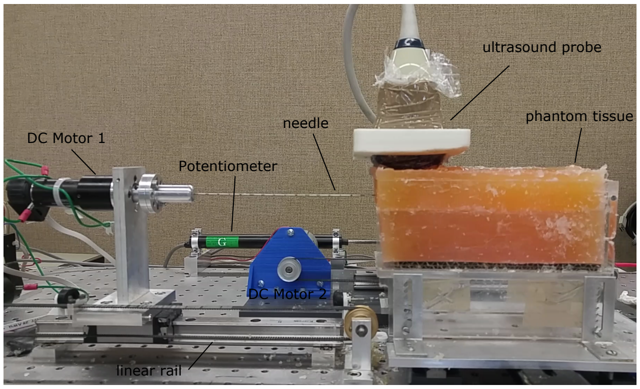

Fig. 2. Needle steering device. A two degree-of-freedom needle insertion robot is used in our experiments. A prismatic joint which controls the needle's insertion velocity is attached to a needle carriage. A rotational joint controls the needle's axial rotation velocity. An ultrasound probe is attached to a separate motor and is used to track the needle tip over the course of the insertion. A potentiometer is used to determine the position of the US probe.

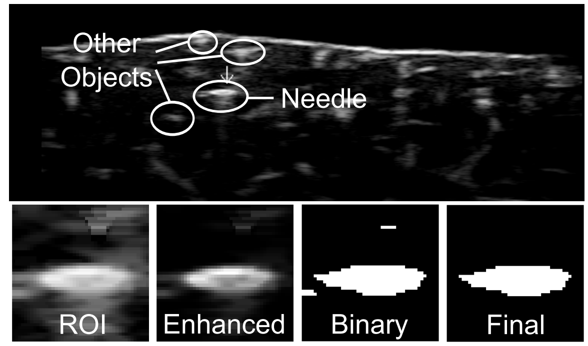

Fig. 3. US image processing steps. The original US image contains the needle, along with other similar objects. First, a ROI is defined around the needle. The image is enhanced, and an appropriate threshold is obtained to produce a binary image. Morphological opening is then used to produce the final image.

IV. Experimental Setup

In this section, we discuss our needle steering device, our ultrasound setup, as well as the tissue phantoms used in our experiments.

A. Needle Steering Device

Our needle steering device consists of a two degree-of-freedom robot, modified from the version described in [34]. A prismatic joint is used to control the needle's insertion velocity while a rotational joint is used to control the needle's axial rotation velocity. The prismatic joint is designed using a ball-bearing mounted needle carriage system attached to a transmission belt. The transmission belt is connected to a Maxon RE40 DC motor (Maxon Motor AG, Sachseln, Switzerland), which controls the needle's linear motion. The rotational joint allows us to adjust the needle's bevel angle during the insertion process using a PID controller. Considering the minimum update time of $T_s = 1$ sec for γ_d, the PID controller is tuned by trial and error to provide a fast response with a settling time of less than one. The revolute joint is powered by a Maxon RE25 1:14 geared motor (Maxon Motor AG, Sachseln, Switzerland). The motors are controlled through Simulink using a Humusoft MF624 DAQ card which interfaces with our PC via PCI connection. An image of the needle steering device is shown in Fig. 2.

A separate motorized prismatic joint is attached to an ultrasound (US) probe holder whose position is monitored using a linear potentiometer. The US probe is controlled such that the needle tip is always in view of the US images. The US probe is positioned such that axial images of the needle are obtained. Axial images observe a cross-section of the needle, causing the needle to appear as a bright elliptical object. A description of our US needle tracking is performed in the next section.

B. US Tracking

US imaging is the most common modality for PPB, and needle insertion procedures in general, due to its accessibility, low cost, and real-time capabilities [35]. In order to track the needle under US feedback, we implemented an image processing algorithm incorporating a dynamic region-of-interest, along with a threshold-based needle tracking approach. The image processing algorithm was first described in [36] and was built off of techniques described in [7] and [37].

A visual overview of the initial US image followed by the subsequent image processing steps is shown in Fig. 3. We then perform contrast enhancement on the ROI to obtain the image labelled "Enhanced". Afterwards, we choose an appropriate intensity threshold for which to produce a binary black-and-white image. In this binary image, the white pixels are expected to correspond to the needle while the black pixels correspond to background tissue. Small, isolated pixel clusters are removed via morphological opening to produce the final image, labelled as "Final".

US images are obtained with a SonixTouch Ultrasound System (Analogic Ultrasound, Richmond, BC, Canada) using a linear US transducer model 4DL14-5/38 (Analogic Ultrasound, Richmond, BC, Canada). The US machine is connected to a PC through a DVI-to-USB 3.0 frame grabber (Epiphan, Palo Alto, CA, USA). The frame grabber obtains US images at a frequency of 20 Hz which are processed using Simulink. A Kalman filter is used to help track the needle during the insertion process and adjust the ROI between each successive frame. Details about the Kalman filter can be found in [36].

C. Tissue and Needle

The experiments are performed on two different types of tissues; phantom tissue and biological tissue. First we used a plastisol sample tissue, which is made of 80% liquid plastic and 20% plastic softener (M-F Manufacturing Co., Fort Worth, TX, USA). The estimated Young's modulus of elasticity of the sample is 35 kPa. Next we performed the experiments on a two-layer biological tissue. The first 40 mm of the tissue is composed of gelatin and the rest is *ex-vivo* beef tissue. This design is intended to simulate the effects of multiple tissue layers. The gelatin layer is made by mixing water at temperature of $70°C$ with porcine gelatin powder (Sigma-Aldrich Co., ON, Canada). The weight ratio of gelatin to water

TABLE I
CONTROLLER PARAMETERS

Subsystem	c_1	c_2	c_3	k_1	k_2	k_3	k_4	k_5
VDC	20	20	100	κ/v	0.1	10	0.1	50
HDC	20	20	100	κ/v	0.1	10	0.1	50

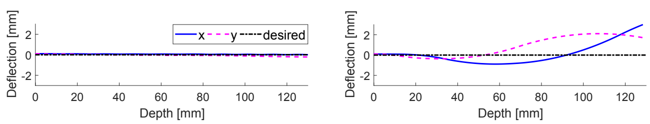

(a) (b)

Fig. 4. The simulation results with initial condition $x_0 = 0.1$, mm $y_0 = 0.1$, mm and $\gamma_0 = 45°$. (a): Results from proposed 3D controller. (b): Results from switching between HDC and VDC based on error magnitude.

mixtures is 15%. The surface of the tissue provides a smooth, consistent surface on which the US probe can slide and ensure good acoustic contact between the US probe and the tissue. In the case of non-flat tissue, the translation and ultrasound probe contact should be taken into account [38]. A standard 18 gauge brachytherapy needle (Eckert & Ziegler BEBIG Inc., Oxford, CT, USA) made of stainless steel was used for each of the insertion trials, and the needle's insertion velocity was held constant at 2 mm/s.

V. RESULTS

The controller we are testing here is the 3D controller (28) to minimize deflection along the x and y axes. This controller considers both axes simultaneously, however, more weight is given to the axes with larger error. In simulations, we also test a 3D steering method, swapping between x and y axes, where only one axes is being controlled. Whenever the deflection along the x axis becomes larger than or equal to that along the y axis, VDC is implemented and whenever the deflection along the y axis is higher, HDC is implemented. In Section V-A, we demonstrate through simulation that our 3D needle steering approach can reduce overall needle deflection. In Section V-B, we use a tissue sample to evaluate the performance of the 3D algorithm via experiments.

A. Simulation Results

Simulations are performed in Matlab/Simulink to test the 3D controller (28) as well as switching between the VDC and HDC controllers based on the larger error. In these simulations, the initial values are selected as $x_0 = 0.1$ mm, $y_0 = 0.1$ mm, and $\gamma_0 = 45°$. The insertion velocity v is 2 mm/sec and the needle curvature κ is selected as 0.0025 mm^{-1} [39]. The value of the controller parameters k_i and $c_i,\ (i = 1, 2, ...)$ are tuned during the simulations by trial and error and later used in the experiments. These values are shown in Table I.

The results are shown in Fig. 4. Comparing the results show that the 3D controller can reduce the error along both axes simultaneously, whereas using HDC and VDC individually is not sufficient.

B. Experimental Results

Here, we demonstrate the performance of the 3D controller using experiments. The experiments are performed on two different tissues and two different scenarios, each for seven trials. In scenario 1, the needle is steered on a straight line to the depth of 130 mm. In scenario 2, the needle is steered to reach a desired final deflection along the x axis and zero deflection along the y axis while inserted to the depth of 130 mm. It should be noted that the proposed 3D controller requires all system states, i.e. position and orientation variables, to be known; however, since our experiment setup can only provide position measurements, the angles α and β are considered to be zero and the angle γ is considered be equal to the needle base angle. This assumption disregards the effects of torsional friction applied to the needle shaft, which should be quite small in practice [28]. Also, the needle is inserted without any initial bending, and the initial bevel angle is set to zero. These assumptions are valid for scenario 1, as for small deflections the orientation angles α and β are close to zero. In scenario 2, due to the needle bending in the x direction the assumption of small orientation angles might not be valid. However, we still use the same assumptions to evaluate the behaviour of the controller. To see the effect of the maximum acceleration, first set of experiments on phantom tissue are performed for the maximum acceleration of 0.99 mm/sec^2 and the second set is performed with the maximum acceleration of 0.71 mm/sec^2. The controller parameters used in the experiments are the same values as simulations shown in Table I. The results are summarized in Table II and one sample trial for each experiment set is shown in Fig. 5 and Fig. 6.

Defining the total error as the Euclidean norm of the error vector, the results for phantom tissue show a maximum mean absolute error of 0.91 mm in scenario 1 and a maximum final error of 1.8 mm in scenario 2. The experiments performed on the biological tissue also show a maximum mean absolute error of 0.57 mm and 2.5 mm in scenario 1 and scenario 2, respectively and a maximum final error of 1.7 mm in scenario 1 and 2.6 mm in scenario 2. Considering scenario 1, the maximum value of error is less than 2 mm which is the size of the smallest lesion that can be detected by ultrasound images [40] and the errors are in the same order as other methods in the literature such as [41].

VI. DISCUSSION

Using the experimental results in Table II, the expected behaviour of the controller can be clearly observed. In scenario 1, by increasing the update time T_s, the deflection error increases. The slower sampling provides less update to the system causing the error to increase. It should be noted that small sample times might also lead to a poor performance due to the delay on error compensation caused by curvature limits. The sample time should be greater than the settling time of the rotation loop to provide the bevel with enough time to reach the desired angle and stay there to compensate for the error. For scenario 2, the effect of the maximum acceleration, or equivalently the maximum bevel angle for each direction

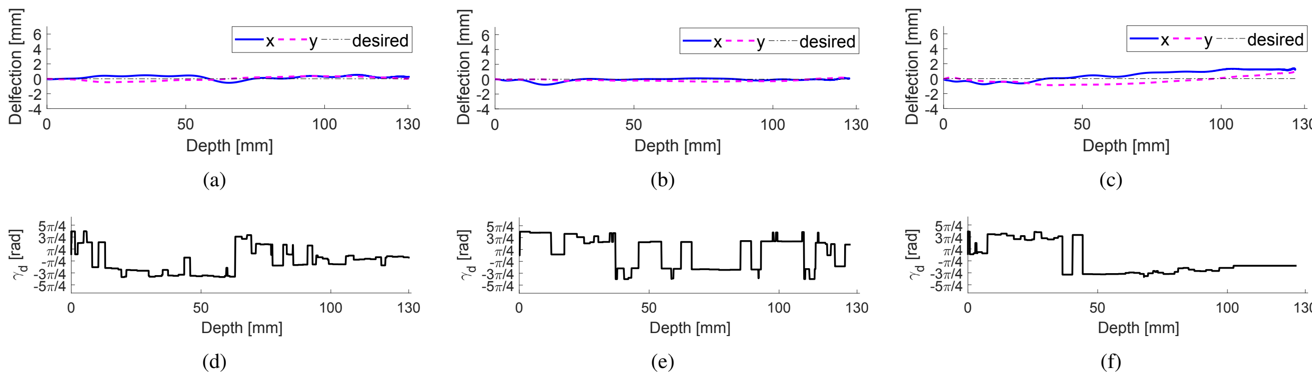

Fig. 5. Samples of experimental results of the 3D controller for steering the needle on a straight line. (a), (d): Insertion in phantom tissue with $T_s = 1$ sec and maximum acceleration of 0.99 mm/sec^2. (b), (e): Insertion in phantom tissue with $T_s = 2$ sec and maximum acceleration of 0.71 mm/sec^2. (c), (f): Insertion in biological tissue with $T_s = 1$ sec and maximum acceleration of 0.99 mm/sec^2.

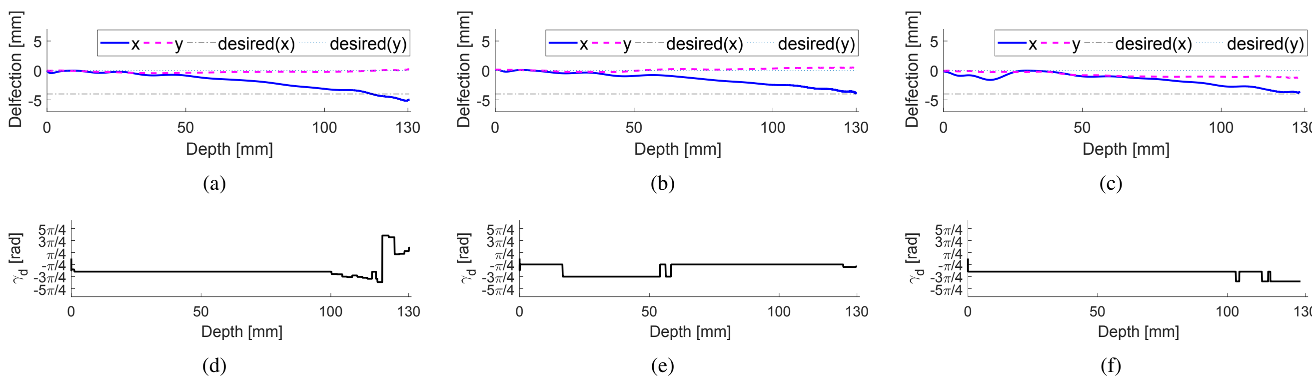

Fig. 6. Samples of experimental results of the 3D controller for steering the needle to the desired deflection of $x_d = -4$ mm along the x-axis and zero deflection along the y-axis. (a), (d): Insertion in phantom tissue with $T_s = 1$ sec and maximum acceleration of 0.99 mm/sec^2. (b), (e): Insertion in phantom tissue with $T_s = 1$ sec and maximum acceleration of 0.71 mm/sec^2. (c), (f): Insertion in biological tissue with $T_s = 1$ sec and maximum acceleration of 0.99 mm/sec^2.

TABLE II
SUMMARY OF THE EXPERIMENTAL RESULTS

			x			y		
Tissue	Scenario	Specification	Mean Absolute Error [mm]	Standard Deviation σ [mm]	Max Final Error [mm]	Mean Absolute Error [mm]	Standard Deviation σ [mm]	Max Final Error [mm]
Phantom Tissue	1	$x_d = 0$ mm, $y_d = 0$ mm, $T_s = 1$ sec, max(γ_d) = 81°	0.37	0.33	0.5	0.25	0.26	0.8
		$x_d = 0$ mm, $y_d = 0$ mm, $T_s = 2$ sec, max(γ_d) = 45°	0.54	0.57	1.7	0.74	0.52	1.05
	2	$x_d = -4$ mm, $y_d = 0$ mm, $T_s = 1$ sec, max(γ_d) = 81°	2.6	1.3	1.1	0.5	0.31	1.5
		$x_d = -4mm$, $y_d = 0$ mm, $T_s = 1$ sec, max(γ_d) = 45°	2.8	1.03	1.1	0.16	0.18	0.54
Biological Tissue	1	$x_d = 0$ mm, $y_d = 0$ mm, $T_s = 1$ sec, max(γ_d) = 81°	0.57	0.45	1.7	0.55	0.48	1.1
	2	$x_d = -4$ mm, $y_d = 0$ mm, $T_s = 1$ sec, max(γ_d) = 81°	2.5	1.1	2.6	0.66	0.44	1.9

can be seen from the experimental results in Table II. For a larger bevel angle, the error along the y direction is smaller since higher acceleration puts more effort to compensate the error along the x axis, which in return has less effect on the y direction. However, by decreasing the bevel angle, the bevel orientation affects the error along the y axis more, causing the error to increase. It should be noted that this discussion is true for the considered case. If the y axis desired deflection is non-zero, the discussion might be different. However, the results verify the expected behaviour. It worth mentioning that in scenario 2, the approximation of the orientation variables might not be accurate and these experiments are only used to understand and verify the behaviour of the controller.

The 3D controller presented here uses the idea presented in [33] to combine the 2D controllers and form the 3D controller. The main difference between these two works is in using different techniques for designing the 2D controllers. Moreover, in [33], the upper bound on the desired angle γ_d is determined by maximum allowed needle bending such that for compensating larger deflections, the upper bound on γ_d should be smaller. This constraint is necessary for guaranteeing the convergence of the error. The controller proposed here does not impose such limitation on the desired angle γ_d as it is only required to choose the maximum acceleration to be less than one, which provides more flexibility in using the system's capacity for compensating the error.

Simulations are provided to compare the proposed controller with the Sliding mode controller proposed by Webster et. al. [25]. The simulations are performed for the two scenarios used in the experiments. The needle rotation velocity for the sliding mode method is selected as 1 rad/sec. The needle curvature, insertion velocity, and all control parameters are the same the values presented in the simulations above. The simulation results are shown in Fig. 7. From these results, we can see that the deflection error behaviour is similar in both methods. Comparing the roll angle γ, the sliding mode method continuously rotates the needle and the variation in this angle is larger when compared to the same quantity in the proposed backstepping control method. The continuous rotation has a drilling effect on tissue, which may increase tissue trauma. In the backstepping method, the needle is rotated only when required and there are times that the needle does not rotate, which reduces the tissue trauma. It should be noted that since the quantitative performance of the method highly depends on the selected parameters, this comparison can only be used to qualitatively compare the performance of these methods.

The model used in this work has only one parameter, the needle path curvature (κ). Having only one parameter limits the effects of parameter uncertainty. The 3D controller structure deals with this uncertainty to some extent as it mainly rotates the needle based on the desired acceleration from both subsystems. If the desired roll angle obtained from the 2D controllers resides in the correct quadrant, the error will decrease. This problem requires further studies to determine the tolerable uncertainty bounds.

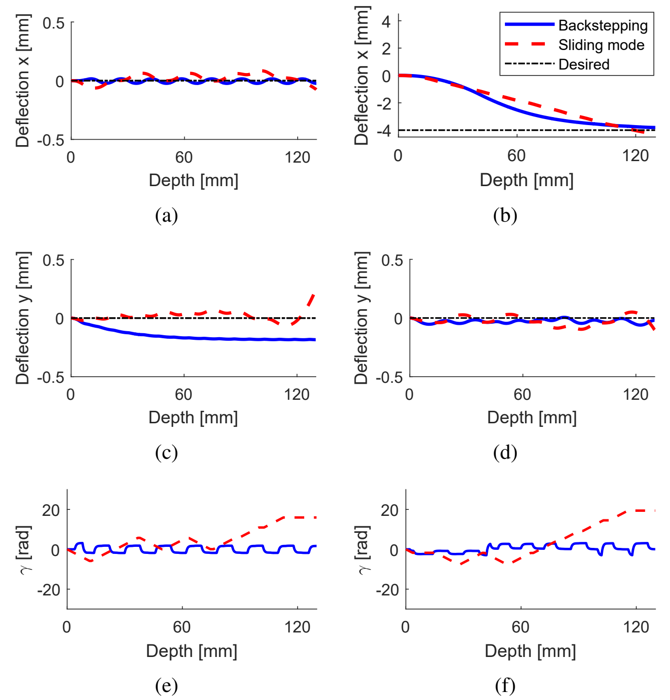

Fig. 7. Simulation results comparing the proposed method with the Sliding mode controller proposed in [25] for the two scenarios. (a),(c),(e): needle deflection and the needle roll angle for moving the needle on a straight line to reach a depth of 130 mm. (b),(d),(f): needle deflection and the needle roll angle for reaching the desired deflection of -4 mm along the x-axis and zero deflection along the y-axis at the depth of 130 mm.

VII. Conclusion

In this paper, we describe a method for controlling needle deflection through the use of multiple 2D planar controllers, each designed using the integrator-backstepping control approach. One controller implements Vertical Deflection Control to reduce needle deflection outside of the $y - z$ plane while the second controller implements Horizontal Deflection Control to reduce deflection outside of the $x - z$ plane. By properly combining the effect of these controllers, we attempt to minimize the overall needle deflection. The proposed 3D controller considers the effect of the error along both x and y axes simultaneously and can guarantee the boundedness of the error. Our needle insertion setup consisted of a two degree-of-freedom surgical robot designed to insert the needle at a constant velocity while adjusting the needle's rotational velocity to allow for needle steering via our derived controllers. Needle insertions were performed using an 18 gauge bevel-tipped brachytherapy needle and a plastisol phantom tissue. Our 3D needle steering approach was able to obtain an average error of less than 1.5 mm.

Future work involves exploration regarding the impact of needle rotation on tissue trauma. As well, we work on improving our 3D needle steering approach by incorporating more accurate ways to estimate α, β, and γ, possibly through the use of state observers.

References

[1] K. K. Charyulu, "Transperineal interstitial implantation of prostate cancer: a new method," *International Journal of Radiation Oncology*

- *Biology - Physics*, vol. 6, no. 9, pp. 1261–1266, 1980.

[2] A. V. Taira, G. S. Merrick, R. W. Galbreath, K. E. Wallner, and W. M. Butler, "Natural history of clinically staged low-and intermediate-risk prostate cancer treated with monotherapeutic permanent interstitial brachytherapy," *International Journal of Radiation Oncology - Biology - Physics*, vol. 76, no. 2, pp. 349–354, 2010.

[3] N. J. Cowan, K. Goldberg, G. S. Chirikjian, G. Fichtinger, R. Alterovitz, K. B. Reed, V. Kallem, W. Park, S. Misra, and A. M. Okamura, "Robotic needle steering: Design, modeling, planning, and image guidance," in *Surgical Robotics*. Springer, 2011, pp. 557–582.

[4] M. Khadem, C. Rossa, R. S. Sloboda, N. Usmani, and M. Tavakoli, "Mechanics of tissue cutting during needle insertion in biological tissue," *IEEE Robotics and Automation Letters*, vol. 1, no. 2, pp. 800–807, July 2016.

[5] C. Rossa, M. Khadem, R. Sloboda, N. Usmani, and M. Tavakoli, "Adaptive quasi-static modelling of needle deflection during steering in soft tissue," *IEEE Robotics and Automation Letters*, vol. 1, no. 2, pp. 916–923, July 2016.

[6] C. Rossa and M. Tavakoli, "Issues in closed-loop needle steering," *Control Engineering Practice*, vol. 62, pp. 55–69, 2017.

[7] Z. Neubach and M. Shoham, "Ultrasound-guided robot for flexible needle steering," *Biomedical Engineering, IEEE Transactions on*, vol. 57, no. 4, pp. 799–805, 2010.

[8] S. P. DiMaio and S. Salcudean, "Needle steering and motion planning in soft tissues," *Biomedical Engineering, IEEE Transactions on*, vol. 52, no. 6, pp. 965–974, 2005.

[9] V. Kallem and N. J. Cowan, "Image guidance of flexible tip-steerable needles," *Robotics, IEEE Transactions on*, vol. 25, no. 1, pp. 191–196, 2009.

[10] M. Motaharifar, H. A. Talebi, F. Abdollahi, and A. Afshar, "Nonlinear adaptive output-feedback controller design for guidance of flexible needles," *IEEE/ASME Transactions on Mechatronics*, vol. 20, no. 4, pp. 1912–1919, 2015.

[11] B. Fallahi, C. Rossa, R. S. Sloboda, N. Usmani, and M. Tavakoli, "Sliding-based switching control for image-guided needle steering in soft tissue," *IEEE Robotics and Automation Letters*, vol. 1, no. 2, pp. 860–867, July 2016.

[12] M. Khadem, C. Rossa, N. Usmani, R. S. Sloboda, and M. Tavakoli, "A two-body rigid/flexible model of needle steering dynamics in soft tissue," *IEEE/ASME Transactions on Mechatronics*, vol. 21, no. 5, pp. 2352–2364, 2016.

[13] D. Glozman and M. Shoham, "Image-guided robotic flexible needle steering," *Robotics, IEEE Transactions on*, vol. 23, no. 3, pp. 459–467, 2007.

[14] S. E. Salcudean, T. D. Prananta, W. J. Morris, and I. Spadinger, "A robotic needle guide for prostate brachytherapy," in *Robotics and Automation, 2008. ICRA 2008. IEEE International Conference on*. IEEE, 2008, pp. 2975–2981.

[15] G. Fichtinger, J. P. Fiene, C. W. Kennedy, G. Kronreif, I. Iordachita, D. Y. Song, E. C. Burdette, and P. Kazanzides, "Robotic assistance for ultrasound-guided prostate brachytherapy," *Medical image analysis*, vol. 12, no. 5, pp. 535–545, 2008.

[16] D. Y. Song, E. C. Burdette, J. Fiene, E. Armour, G. Kronreif, A. Deguet, Z. Zhang, I. Iordachita, G. Fichtinger, and P. Kazanzides, "Robotic needle guide for prostate brachytherapy: clinical testing of feasibility and performance," *Brachytherapy*, vol. 10, no. 1, pp. 57–63, 2011.

[17] G. J. Vrooijink, M. Abayazid, S. Patil, R. Alterovitz, and S. Misra, "Needle path planning and steering in a three-dimensional non-static environment using two-dimensional ultrasound images," *The International Journal of Robotics Research*, pp. 1–14, 2014.

[18] T. K. Adebar, A. E. Fletcher, and A. M. Okamura, "3-D ultrasound-guided robotic needle steering in biological tissue," *Biomedical Engineering, IEEE Transactions on*, vol. 61, no. 12, pp. 2899–2910, 2014.

[19] J. Van Den Berg, S. Patil, R. Alterovitz, P. Abbeel, and K. Goldberg, "LQG-based planning, sensing, and control of steerable needles," in *Algorithmic Foundations of Robotics IX*. Springer, 2011, pp. 373–389.

[20] K. B. Reed, V. Kallem, R. Alterovitz, K. Goldbergxz, A. M. Okamura, and N. J. Cowan, "Integrated planning and image-guided control for planar needle steering," in *Biomedical Robotics and Biomechatronics, 2008. BioRob 2008. 2nd IEEE RAS & EMBS International Conference on*. IEEE, 2008, pp. 819–824.

[21] T. R. Wedlick and A. M. Okamura, "Characterization of pre-curved needles for steering in tissue," in *Engineering in Medicine and Biology Society, 2009. EMBC 2009. Annual International Conference of the IEEE*. IEEE, 2009, pp. 1200–1203.

[22] P. E. Dupont, J. Lock, B. Itkowitz, and E. Butler, "Design and control of concentric-tube robots," *Robotics, IEEE Transactions on*, vol. 26, no. 2, pp. 209–225, 2010.

[23] D. C. Rucker, R. J. Webster, G. S. Chirikjian, and N. J. Cowan, "Equilibrium conformations of concentric-tube continuum robots," *The International journal of robotics research*, 2010.

[24] R. J. Webster and B. A. Jones, "Design and kinematic modeling of constant curvature continuum robots: A review," *The International Journal of Robotics Research*, 2010.

[25] D. C. Rucker, J. Das, H. B. Gilbert, P. J. Swaney, M. I. Miga, N. Sarkar, and R. J. Webster, "Sliding mode control of steerable needles," *Robotics, IEEE Transactions on*, vol. 29, no. 5, pp. 1289–1299, 2013.

[26] D. S. Minhas, J. A. Engh, M. M. Fenske, and C. N. Riviere, "Modeling of needle steering via duty-cycled spinning," in *Engineering in Medicine and Biology Society, 2007. EMBS 2007. 29th Annual International Conference of the IEEE*. IEEE, 2007, pp. 2756–2759.

[27] K. Yan, W. S. Ng, K. V. Ling, T.-I. Liu, Y. Yu, and T. Podder, "High frequency translational oscillation & rotational drilling of the needle in reducing target movement," in *Computational Intelligence in Robotics and Automation, 2005. CIRA 2005. Proceedings. 2005 IEEE International Symposium on*. IEEE, 2005, pp. 163–168.

[28] R. J. Webster, J. S. Kim, N. J. Cowan, G. S. Chirikjian, and A. M. Okamura, "Nonholonomic modeling of needle steering," *The International Journal of Robotics Research*, vol. 25, no. 5-6, pp. 509–525, 2006.

[29] M. Waine, C. Rossa, N. Usmani, R. Sloboda, and M. Tavakoli, "An integrator-backstepping control approach for out-of-plane needle deflection minimization," in *Advanced Intelligent Mechatronics (AIM), 2016 IEEE International Conference on*. IEEE, 2016, pp. 1598–1603.

[30] H. D. Taghirad, *Parallel robots: mechanics and control*. CRC press, 2013.

[31] H. K. Khalil and J. Grizzle, *Nonlinear systems*. Prentice hall New Jersey, 1996, vol. 3.

[32] A. D. Ames, X. Xu, J. W. Grizzle, and P. Tabuada, "Control barrier function based quadratic programs for safety critical systems," *IEEE Transactions on Automatic Control*, vol. 62, no. 8, pp. 3861–3876, 2017.

[33] B. Fallahi, C. Rossa, R. S. Sloboda, N. Usmani, and M. Tavakoli, "Sliding-based image-guided 3D needle steering in soft tissue," *Control Engineering Practice*, vol. 63, pp. 34–43, 2017.

[34] T. Lehmann, C. Rossa, N. Usmani, R. Sloboda, and M. Tavakoli, "A virtual sensor for needle deflection estimation during soft-tissue needle insertion," in *Robotics and Automation (ICRA), 2015 IEEE International Conference on*. IEEE, 2015, pp. 1217–1222.

[35] P. C. Mozer, A. W. Partin, and D. Stoianovici, "Robotic image-guided needle interventions of the prostate," *Rev. Urol*, vol. 11, no. 1, pp. 7–15, 2009.

[36] M. Waine, C. Rossa, R. Sloboda, N. Usmani, and M. Tavakoli, "Needle tracking and deflection prediction for robot-assisted needle insertion using 2D ultrasound images," *Journal of Medical Robotics Research*, vol. 01, no. 01, p. 1640001, 2016. [Online]. Available: http://www.worldscientific.com/doi/abs/10.1142/S2424905X16400018

[37] P. Yan, J. C. Cheeseborough, and K. C. Chao, "Automatic shape-based level set segmentation for needle tracking in 3-d TRUS-guided prostate brachytherapy," *Ultrasound in medicine & biology*, vol. 38, no. 9, pp. 1626–1636, 2012.

[38] M. Abayazid, P. Moreira, N. Shahriari, S. Patil, R. Alterovitz, and S. Misra, "Ultrasound-guided three-dimensional needle steering in biological tissue with curved surfaces," *Medical engineering & physics*, vol. 37, no. 1, pp. 145–150, 2015.

[39] M. Khadem, C. Rossa, N. Usmani, R. S. Sloboda, and M. Tavakoli, "Robotic-assisted needle steering around anatomical obstacles using notched steerable needles," *IEEE journal of biomedical and health informatics*, vol. 22, no. 6, pp. 1917–1928, 2018.

[40] P. Moreira and S. Misra, "Biomechanics-based curvature estimation for ultrasound-guided flexible needle steering in biological tissues," *Annals of biomedical engineering*, vol. 43, no. 8, pp. 1716–1726, 2015.

[41] A. Krupa, "3D steering of a flexible needle by visual servoing," in *International Conference on Medical Image Computing and Computer-Assisted Intervention*. Springer, 2014, pp. 480–487.

Bita Fallahi received her BSc and MSc degrees in electrical engineering from K.N. Toosi University of Technology, Iran, in 2007 and 2011, respectively. She earned her PhD degree in Control Systems from the University of Alberta in 2018, focusing on control of robot-assisted minimally invasive surgery. Her current research interests include medical robotics and image-guided surgery.

Michael Waine received his Master's degree in biomedical engineering at the University of Alberta in 2015. He focused on robot-assisted prostate cancer during his graduate research, with a special interest in biomedical imaging and control systems. He is now attending medical school at the University of British Columbia.

Carlos Rossa is an Assistant Professor of Mechatronics in the Faculty of Engineering and Applied Science at Ontario Tech University. He received his BEng and MSc degrees in Mechanical Engineering from the Ecole Nationale d'Ingnieurs de Metz, Metz, France, both in 2010, and earned his PhD degree in Mechatronics and Robotics from the Universit Pierre et Marie Curie, Paris, France, in 2013, under the auspices of the French Atomic Energy Commission (CEA). From 2014 to 2017, he was a postdoctoral fellow at the University of Alberta, Canada. His research interests include medical robotics and imaging systems

Ron S. Sloboda received the B.Sc. degree in physics from the University of Manitoba, Winnipeg, MB, Canada, in 1974, and the Ph.D. degree in physics, nuclear theory, from the University of Alberta, Edmonton, AB, Canada, in 1979. He is currently a Professor in the Department of Oncology, University of Alberta. His research interests include dosimetry and treatment planning for brachytherapy, including the design of clinical studies to obtain patient data and model based dose calculation.

Nawaid Usmani is an Associate Professor as a Radiation Oncologist at the University of Alberta. His practice is based on treating genito-urinary malignancies and gastro-intestinal malignancies. Dr. Usmani's main focus on research is in prostate brachytherapy. Currently, prostate brachytherapy is an increasingly popular treatment option for localized prostate cancer due to its excellent efficacy, good toxicity profile and convenience. However, there remains a great deal of potential to improve the current technique. Dr. Usmani's main objective for this research is to characterize current brachytherapy techniques and identify strategies for improving this treatment. This includes quantifying inaccuracies in current brachytherapy techniques, identifying patient populations at a higher risk of toxicity from this treatment, and finding ways to improve our outcomes with brachytherapy implants (using technical and translational approaches). In addition to this research in prostate brachytherapy, Dr. Usmani is involved in a number of other research endeavours. His other research includes: Investigating the potential benefits of metformin in preventing metabolic complications of hormonal therapy and improving prostate cancer outcomes, identifying new prognostic or predictive biomarkers in prostate cancer, investigating the utility of magnetic resonant imaging and PET imaging in the management of prostate cancer, investigating the potential benefits of exercise in rectal cancer patients.

Mahdi Tavakoli is a Professor in the Department of Electrical and Computer Engineering, University of Alberta, Canada. He received his BSc and MSc degrees in Electrical Engineering from Ferdowsi University and K.N. Toosi University, Iran, in 1996 and 1999, respectively. He received his PhD degree in Electrical and Computer Engineering from the University of Western Ontario, Canada, in 2005. In 2006, he was a post-doctoral researcher at Canadian Surgical Technologies and Advanced Robotics (CSTAR), Canada. In 2007-2008, he was an NSERC Post-Doctoral Fellow at Harvard University, USA. Dr. Tavakolis research interests broadly involve the areas of robotics and systems control. Specifically, his research focuses on haptics and teleoperation control, medical robotics, and image-guided surgery. Dr. Tavakoli is the lead author of Haptics for Teleoperated Surgical Robotic Systems (World Scientific, 2008). He is an Associate Editor for IEEE/ASME Transactions on Mechatronics, Journal of Medical Robotics Research, Control Engineering Practice, and Mechatronics.